Review Vol. 12, No. 12 / 1 Dec 2022 / Optical Materials Express 4528
Optical Materials EXPRESS

Graphene metasurfaces for terahertz wavefront shaping and light emission [Invited]

YUYU LI, MATHAN RAMASWAMY KRISSHNAMURTHI, WEIJUN LUO, ANNA K. SWAN, XI LING, AND ROBERTO PAIELLA*

Department of Electrical and Computer Engineering and Photonics Center, Boston University, 8 Saint Mary's Street, Boston, MA 02215, USA
*rpaiella@bu.edu

Abstract: Graphene is a promising materials platform for metasurface flat optics at terahertz wavelengths, with the important advantage of active tunability. Here we review recent work aimed at the development of tunable graphene metasurfaces for THz wavefront shaping (including beam-steering metamirrors and metalenses) and light emission. Various design strategies for the constituent meta-units are presented, ranging from metallic phase-shifting elements combined with a nearby graphene sheet for active tuning to graphene plasmonic resonators providing the required phase control or radiation mechanism. The key challenge in the development of these devices, related to the limited radiative coupling of graphene plasmonic excitations, is discussed in detail together with recently proposed solutions. The resulting metasurface technology can be expected to have a far-reaching impact on a wide range of device applications for THz imaging, sensing, and future wireless communications.

© 2022 Optica Publishing Group under the terms of the Optica Open Access Publishing Agreement

1. Introduction

Metasurfaces are poised to have a major technological impact on a variety of disciplines ranging from imaging and sensing to communications and beyond. Typical metasurface architectures consist of ordered two-dimensional arrays of metallic or dielectric nanoparticles of variable size, shape, and orientation, designed to introduce a desired phase, amplitude, and/or polarization profile on incident light [1–3]. This basic capability is attractive for a multitude of passive device applications, such as image formation, polarization control, and holography, with the advantage of enhanced miniaturization and functionality. More recently, the integration of similar metasurfaces with active optoelectronic materials and devices (particularly light emitters [4–8]) has also started to receive increasing attention, driven by similar considerations.

Regardless of the application, the accessible spectral range is largely dictated by the material choice for the metasurface building blocks (meta-atoms), with noble metals and dielectrics generally preferable for near-infrared and visible wavelengths, respectively. For operation at longer wavelengths, graphene has recently emerged as a particularly promising materials platform. It is well established that graphene plasmon polaritons (GPPs) can provide strong optical confinement at mid-infrared and terahertz wavelengths, with favorable propagation characteristics compared to surface plasmons in noble metals [9–15]. Furthermore, the dynamic conductivity, and therefore optical response, of graphene can be tuned actively with a gate voltage in a standard field-effect-transistor (FET) configuration. Therefore, the use of graphene meta-atoms could also allow for the development of reconfigurable and dynamically switchable metasurface devices, which are otherwise challenging to engineer with more traditional materials systems [16].

This review article is focused on the design and operating principles of graphene THz metasurfaces for wavefront control and light emission. Compared to their near-infrared and visible counterparts, THz metasurfaces in general have so far received more limited attention, with initial reports based on metallic resonant circuit elements, dielectric resonators, or MEMS [17–22]. At the same time, the development of such metasurfaces could help address the current

#473110 https://doi.org/10.1364/OME.473110
Journal © 2022 Received 16 Aug 2022; revised 29 Sep 2022; accepted 18 Oct 2022; published 7 Nov 2022

Optical Materials EXPRESS

lack of suitable devices for a wide range of well-established sensing and imaging applications of THz light [23,24]. Furthermore, the ongoing push towards higher and higher frequencies for wireless communications beyond 5G [25] provides a compelling new motivation for the exploration of novel THz devices for wavefront engineering.

The remainder of the article is organized as follows. In the next section, we introduce the dynamic conductivity that governs the optical response of graphene (section 2.1) and use it to describe the plasmonic properties of graphene films (2.2) and micro/nanostructures (2.3), and to discuss the accessible phase tuning range of GPP resonances (2.4). We also identify the range of THz frequencies where the optical response is dominated by plasmonic excitations, below which graphene essentially behaves as a tunable non-resonant loss element. In section 3, we review prior work on graphene metasurfaces for wavefront control, including tunable metamirrors and metalenses. Specifically, first we consider low-frequency devices where a sheet of graphene is simply used to tune the response of an adjacent metallic metasurface (section 3.1). Next (3.2), we describe patterned graphene metasurfaces where each meta-atom supports a localized plasmonic resonance with geometrically and actively tunable phase response. The latter devices have not been demonstrated experimentally yet, despite numerous theoretical proposals, due to materials limitations of existing large-area graphene samples. At the end of section 3.2, a structure that allows circumventing these limitations is also presented, based on meta-atoms designed to maximize the GPP coupling to radiation. In section 4, we review the recent demonstration of THz light-emitting metasurfaces, where GPPs in nanoribbons are electrically excited and then radiate at their resonance frequency. Common design requirements between these devices and the wavefront-shaping metasurfaces of the previous section are also outlined. Finally, our conclusions and outlook of this growing area of research are presented in section 5.

2. Graphene terahertz response

2.1. Surface conductivity

Graphene is a single layer of carbon atoms arranged in a honeycomb lattice. Because of its ultrasmall thickness, its optical response is most conveniently described (both conceptually and for numerical modeling) in terms of a two-dimensional surface conductivity $\sigma(\omega, \boldsymbol{\beta})$, where ω and $\boldsymbol{\beta}$ indicate, respectively, the angular frequency and wavevector of the incident electric field. A particularly simple expression is obtained with the Drude model [26,27], which assumes negligible wave retardation (i.e., β much larger than the free-space wavenumber $k_0 = \omega/c$), degenerate doping (i.e., Fermi energy E_F much larger than the thermal energy $k_B T$), and small enough frequency (less than $2E_F/\hbar$) so that interband transitions are forbidden by Pauli blocking. Under these conditions, which generally apply to all the devices described below,

$$\sigma(\omega) = \frac{q^2 E_F}{\pi\hbar^2} \frac{\tau}{1 - i\omega\tau}, \tag{1}$$

where q is the electron charge and τ is the relaxation lifetime accounting for all the relevant electronic scattering mechanisms (impurities, defects, phonons, etc.).

It follows from Eq. (1) that the graphene response to an incident optical field depends on two key material parameters, i.e., E_F and τ. The dependence on Fermi energy is what endows graphene with its distinctive electrostatic tunability of absorption and refraction. Specifically, in the standard FET configuration [Fig. 1(a)], the graphene carrier density N is controlled by the gate voltage V_G according to the capacitor relation $qN = C(V_G - V_{CNP})$, where V_{CNP} is the gate voltage at charge neutrality and C is the FET capacitance. The detailed relationship between E_F and N in a crystalline solid generally depends on the electronic band structure. In graphene, the conical dispersion near the Dirac points yields $E_F = \hbar v_F \sqrt{\pi N}$ [28], where $v_F \approx 1 \times 10^8$ cm/s is the Fermi velocity. The conductivity of Eq. (1) is therefore electrostatically tunable with a square-root dependence on the gate voltage $V_G - V_{CNP}$.

Optical Materials EXPRESS

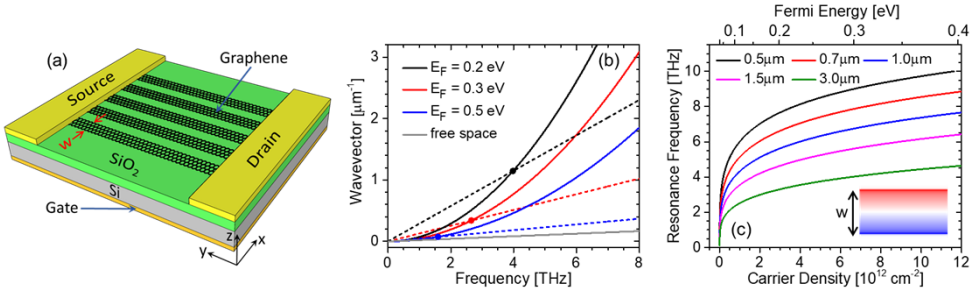

Fig. 1. Graphene plasmon polaritons. (a) Schematic illustration of a graphene ribbon array in a standard FET configuration. (b) Real part (solid lines) and imaginary part (dashed lines) of the GPP wavevector β versus frequency, computed using Eq. (3) for different values of the graphene Fermi energy. For simplicity, here the substrate is modeled with a constant permittivity $\varepsilon_r = 3.9$. The grey line shows the dispersion curve of light in free space. The circles show the intersection points between the real and imaginary parts of β. (c) Plasmonic resonance frequency ν_1 of a graphene ribbon versus carrier density N (bottom axis) and Fermi energy (top axis), computed using Eq. (4) for different values of the ribbon width w. Inset: FDTD simulation results for the z component of the electric field on the ribbon plane under normal-incidence plane-wave excitation at frequency ν_1. Blue, white, and red indicate positive, zero, and negative field amplitude, respectively.

An important question for many graphene devices (including the metasurfaces described below) is related to the practical tuning range of E_F. In general, the maximum accessible gate voltage is limited by electrostatic breakdown in the gate dielectric. In large-area graphene plasmonic devices on Si/SiO_2 substrates, Fermi energies up to about 0.45 eV have been reported with $V_G - V_{CNP} = 210$ V [29]. Similar values were also obtained with an ion-gel top gate dielectric at a much smaller (two orders of magnitude) gate voltage [30]. Recent work has also established that the doping range can be significantly enhanced in double-layer graphene stacks, assembled through the consecutive transfer of two single-layer sheets [31,32]. Specifically, it has been shown that the plasmonic response of a double-layer sample of total carrier density N is equivalent to that of a single layer with an effective Fermi energy $\tilde{E}_F$ that can be substantially larger (by up to a factor of $\sqrt{2}$) than that of an actual single-layer sheet with the same carrier density N. Based on these considerations, we can identify a maximum accessible Fermi energy of about 0.6 eV for the type of devices considered below. On the opposite end, a minimum practical value of about 0.1 eV also exists due to inevitable charge puddles from substrate impurities [33], which can wash out plasmonic effects [34].

The other key material parameter that affects the graphene optical response is the relaxation lifetime τ, which can be evaluated in terms of the electrical mobility μ obtained from transport measurements. Specifically, by combining the Drude conductivity model of Eq. (1) with the standard formula for the static conductivity $\sigma(\omega=0) = q\mu N$, one finds

$$\mu = q v_F^2 \tau / E_F. \tag{2}$$

It is well established that high-quality exfoliated graphene samples can feature exceptionally high room-temperature mobility, ranging from about 10,000 $cm^2/V/s$ on oxidized Si substrates [35] to over 100,000 $cm^2/V/s$ when partially suspended [36] or embedded within highly inert hexagonal-BN layers [37]. Unfortunately, such samples are generally limited to lateral dimensions of a few 10 μm (smaller than the free-space wavelength at THz frequencies), whereas the device applications described below require active areas of a few mm^2. Currently, such dimensions are only accessible with samples grown by chemical vapor deposition (CVD) and transferred to the target substrate with a polymer support film. For devices on standard Si/SiO_2 substrates assembled

Optical Materials EXPRESS

with the commonly used poly(methyl methacrylate) (PMMA)-assisted process, mobilities in the range of 1,000 to 2,000 $cm^2/V/s$ are typically obtained [38]. For a reasonably large Fermi energy $E_F = 0.4$ eV, the corresponding lifetime τ ranges between 40 and 80 fs. Finally, we note that an important recent development is the demonstration of significantly larger mobilities (by a factor of over 4) in CVD-graphene samples produced with less established transfer methods [39] and carefully optimized growth processes [40].

2.2. Plasmonic dispersion in two dimensions

To describe the plasmonic properties of graphene, we begin by considering an infinite planar sheet surrounded by two dielectric media of relative permittivities ε_{r1} and ε_{r2}. This system supports a continuous distribution of plasmon polariton modes, which can be computed by solving Maxwell's equations in the space immediately below and above the sheet for an optical wave of frequency ω and in-plane wavevector $\boldsymbol{\beta}$, and then applying the electromagnetic boundary conditions. If the graphene surface conductivity is modeled with the Drude expression of Eq. (1), the following dispersion relation is obtained for the GPPs [27]

$$\beta(\omega) = \frac{\pi\hbar^2\epsilon_0(\varepsilon_{r1} + \varepsilon_{r2})}{q^2 E_F}\left(1 + \frac{i}{\omega\tau}\right)\omega^2. \tag{3}$$

A more accurate result (valid for arbitrary doping levels and non-equilibrium carrier distributions) can be constructed by evaluating the electronic polarizability in the random phase approximation and then computing the zeros of the resulting dielectric function [27,41,42].

The solid and dashed lines in Fig. 1(b) show, respectively, the real and imaginary parts of β from Eq. (3) plotted as a function of frequency for a graphene sheet on oxidized silicon with $\mu = 2{,}000$ $cm^2/V/s$ and different values of E_F. As illustrated in this figure, the GPP propagation constant $\mathrm{Re}[\beta(\omega)]$ can be larger than the free-space wavenumber $k_0 = \omega/c$ (grey line) by over an order of magnitude. As a result, the wavelength and transverse localization length of GPPs can be smaller than the free-space wavelength by the same factor, leading to extreme optical confinement. An obvious consequence of this wavelength mismatch is the inability to excite GPPs directly with incident radiation. Therefore, the experimental observation of GPPs in two-dimensional samples requires a suitable intermediary excitation mechanism, such as evanescent coupling with a nanotip [43,44] or diffraction by a periodic grating [29,34,45–48].

Equation (3) and Fig. 1(b) also show that the quality factor of these plasmonic oscillations (determined by the ratio $\mathrm{Re}[\beta(\omega)]/\mathrm{Im}[\beta(\omega)] = \omega\tau$) becomes less than one at optical frequencies $\nu = \omega/(2\pi)$ smaller than $\nu_c = 1/(2\pi\tau)$. This cutoff frequency [indicated by the circles in Fig. 1(b)] therefore represents an effective lower bound for the accessible spectral range of graphene plasmonics. At lower frequencies [where the real part of the surface conductivity of Eq. (1) becomes larger than the imaginary part], graphene instead increasingly behaves as a purely lossy conductor. Correspondingly, its electromagnetic response is dominated by free-carrier absorption, with no resonant behavior but still actively tunable with a gate voltage.

2.3. Plasmonic resonances in micro/nanostructures

Metasurfaces generally comprise dense arrays of sub-wavelength meta-atoms, each designed to impart a desired local phase shift to the incident radiation field. By virtue of their large propagation constant $\mathrm{Re}[\beta(\omega)] >> k_0$ (i.e., large effective index), GPPs are ideally well suited to implement this functionality. The required lateral spatial confinement and resonant behavior can be obtained by patterning the graphene sheet into suitably shaped micro- or nanostructures. A particularly important example is the ribbon geometry shown in Fig. 1(a), which can be readily connected between the source and drain contacts in a FET for gating and, if needed, current injection.

Optical Materials EXPRESS

In this geometry, GPPs bounce back and forth between the ribbon edges, and plasmonic resonances are produced via constructive interference upon each roundtrip – i.e., when the phase condition $2\mathrm{Re}[\beta_x]w + 2\varphi_r = 2n\pi$ is satisfied. Here β_x indicates the GPP wavevector component perpendicular to the ribbon, w is the ribbon width, n is a positive integer, and φ_r is the GPP reflection phase at the ribbon edges (for which a nontrivial value of about $\pi/4$ has been computed [49]). Combining this phase condition with Eq. (3), one obtains the following expression for the plasmonic resonance frequencies $\nu_n = \omega_n/(2\pi)$:

$$\nu_n = \frac{1}{2\pi}\sqrt{\frac{q^2 v_F(n\pi - \varphi_r)}{\sqrt{\pi}\hbar\epsilon_0(\epsilon_{r1} + \epsilon_{r2})}}\frac{N^{1/4}}{\sqrt{w}}. \tag{4}$$

More specifically, this equation describes the ribbon plasmonic modes with zero longitudinal wavevector β_y. For each value of the index n, a continuous distribution of GPPs with nonzero β_y also exist that propagate along the ribbon in the y direction. However, the resulting plasmonic density of modes is peaked at the resonance frequencies of Eq. (4) [50], so that the ribbon optical response is typically dominated by the GPPs at these frequencies. As illustrated in Fig. 1(c), by varying the ribbon width w and carrier density N, the fundamental resonance ν_1 can be tuned across the entire THz range (and beyond for narrower ribbons).

The properties of graphene-ribbon plasmonic excitations have been studied extensively in several experimental reports [30,51–53], including their geometric and electrostatic tunability and their hybridization with surface optical phonons in an underlying SiO_2 film. These resonant modes can be excited directly by incident light due to the relaxed requirement of momentum conservation in the ribbon geometry. However, their coupling to radiation Γ_{rad} is still limited by the large mismatch between the ribbon width and the free-space wavelength, which represents a key challenge for the devices described in this article. It should also be noted that, because of the transverse-magnetic (TM) nature of GPPs, the resonant modes of Eq. (4) can only be excited by light polarized perpendicular to the ribbons.

Fully discrete GPP resonances can similarly be achieved in two-dimensional nanostructures such as disks [54–56] and rings [57]. These configurations allow for additional design flexibility, polarization-independent response, and the possibility of phase control via the Pancharatnam-Berry effect [58] as described below. However, active tuning by electrostatic doping is more challenging, as it requires either a conductive substrate immediately below the graphene nanostructures [57] or narrow graphene channels connecting adjacent meta-atoms [56].

2.4. Resonance phase tuning

A key requirement for the building blocks of wavefront-shaping metasurfaces is the ability to tune their reflection or transmission phase across the entire 2π range by varying their geometry (or Fermi energy in the case of graphene). The ribbon GPPs are dipolar resonances [see inset of Fig. 1(c)] with a Lorentzian response, where the phase excursion across the spectral linewidth is fundamentally limited to a maximum value of π. When the resonance frequency of Eq. (4) is shifted by changing the ribbon width or Fermi energy, the resulting phase variations at any given frequency are therefore limited to the same range. Importantly, however, this range can be doubled if the ribbons are placed on a perfectly reflecting substrate so that the incident light interacts with the GPP resonance twice.

These ideas can be formalized using the coupled-mode theory (CMT) framework [59], where the energy stored in a resonance is evaluated based on the interplay between nonradiative dissipation (i.e., absorption) at a rate Γ_{nr} and coupling to incident and outgoing light at a rate Γ_{rad}. For a resonant system on a perfect reflector, this model produces the following expression for the amplitude reflection coefficient [60]

$$r = -1 + \frac{2\Gamma_{rad}}{\Gamma_{rad} + \Gamma_{nr} - i(\omega - \omega_0)}, \tag{5}$$

Optical Materials EXPRESS

where ω_0 is the resonance angular frequency. The frequency dependence of this parameter is illustrated for different values of Γ_{rad}/Γ_{nr} in the Smith chart of Fig. 2(a), where each trace crosses the horizontal axis at ω_0 with ω varying from 0 to ∞ in the counterclockwise direction. Three distinct regimes can be identified in this plot. For $\Gamma_{rad} < \Gamma_{nr}$ (under-coupling), the real part of r is negative at all frequencies, and as a result the phase tuning range is again limited to less than π. For $\Gamma_{rad} = \Gamma_{nr}$ (critical coupling), perfect absorption with $r = 0$ is obtained at resonance. For $\Gamma_{rad} > \Gamma_{nr}$ (over-coupling), the Smith curve spans all four quadrants so that a tuning range of 2π can be achieved. The full extent of this range is then limited by the finite imaginary part of r at $\omega = 0$, which is inversely related to the quality factor $\omega_0/(\Gamma_{rad} + \Gamma_{nr})$. For comparison, Fig. 2(b) shows the Smith chart of the same resonant system embedded in a perfectly transparent homogeneous medium (with no reflector), where the reflection coefficient is $r = -\Gamma_{rad}/[\Gamma_{rad} + \Gamma_{nr} - i(\omega - \omega_0)]$ and the phase excursion is less than π for all values of Γ_{rad}/Γ_{nr}.

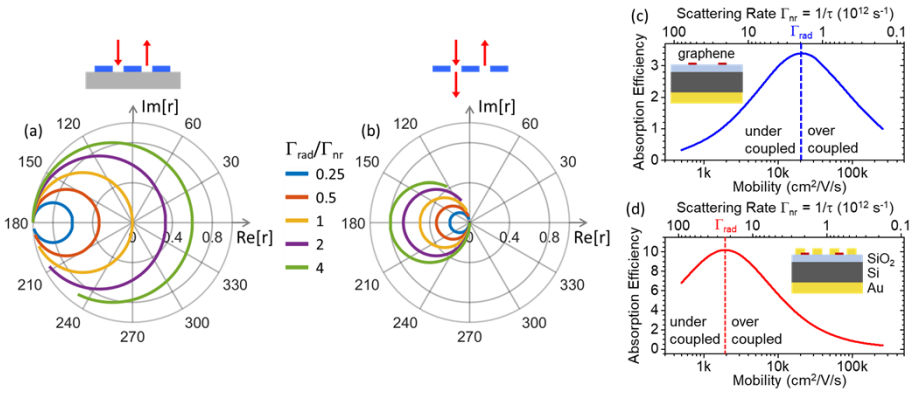

Fig. 2. Resonance phase tuning of graphene plasmonic oscillators. (a) Reflectance Smith chart for a generic resonant system on a perfect mirror, computed with CMT for $\Gamma_{nr} = \omega_0/8$ and different values of Γ_{rad}. (b) Reflectance Smith chart for the same system embedded in a transparent homogeneous medium. (c), (d) Absorption efficiency of the structures shown in the insets versus graphene mobility μ (bottom axis) and GPP nonradiative scattering rate $\Gamma_{nr} = 1/\tau$ (top axis), for an incident light frequency of 3 THz and a graphene Fermi energy E_F of 0.3 eV. Panel (c) corresponds to a periodic array of double-layer graphene ribbons on a Si/SiO_2 substrate with a Au back mirror. Panel (d) corresponds to a similar system where the ribbons are coupled to Au antennas. In both structures, the geometrical parameters were selected to maximize the GPP absorption at a peak frequency of 3 THz [61]. The vertical dashed lines indicate the mobilities required for critical coupling. (c), (d) Adapted from Ref. 61, Copyright (2021), Optica Publishing Group.

CVD-graphene plasmonic resonators are generally under-coupled, as illustrated in Fig. 2(c) for a ribbon array on a Si/SiO_2 substrate with a Au back reflector [61]. With the proper choice of Si/SiO_2 thickness (approximately a quarter wavelength), this structure behaves like the ideal one-port system of Fig. 2(a), with maximum absorption at critical coupling [62,63]. Figure 2(c) shows finite-difference time-domain (FDTD) simulation results for the ribbon plasmonic absorption efficiency at resonance, plotted as a function of mobility μ (bottom axis) and nonradiative relaxation rate Γ_{nr} (top axis). In graphene, nonradiative GPP damping involves the same scattering processes responsible for limiting the mobility, so that $\Gamma_{nr} = 1/\tau$, which is inversely proportional to μ according to Eq. (2). As shown by the dashed vertical line in Fig. 2(c), in this device the critical-coupling condition (where $\Gamma_{rad} = \Gamma_{nr}$) occurs at an exceedingly large mobility of over 20,000 $cm^2/V/s$. As a result, for typical mobilities of CVD graphene (up to ~2,000 $cm^2/V/s$), $\Gamma_{rad} << \Gamma_{nr}$ and therefore the ribbons are in the under-coupled regime where the phase tuning range is below π.

Optical Materials EXPRESS

This discussion highlights the key design challenge for graphene plasmonic metasurfaces, i.e., increasing the radiative decay rate Γ_{rad} so that over-coupling can be achieved with practical CVD samples. This challenge can be addressed by combining the graphene plasmonic resonators with metallic antennas that can effectively mediate the large wavelength mismatch between free-space radiation and GPPs [64–68]. To illustrate, in Fig. 2(d) we consider a structure where the ribbons on the Au/Si/SiO_2 cavity are interspersed with Au rectangular patches, designed to support weakly confined resonances near the graphene plasmonic frequency [61]. The FDTD simulation results shown in this figure indicate that, with this arrangement, the over-coupled regime is already achieved at mobilities accessible with CVD samples, where the phase tuning range can therefore exceed the under-coupled π limit.

3. Graphene metasurfaces for tunable THz wavefront shaping

3.1. Graphene loss modulation in metallic metasurfaces

In this section, we review recent work on low-frequency ($\lesssim$ 1 THz) metallic metasurfaces where a continuous sheet of graphene is used as an active tuning element. As mentioned above, in this frequency range GPPs are generally quite weak, and the graphene optical response is dominated by non-resonant gate-tunable free-carrier absorption. Therefore, if a graphene sheet is inserted in the near-field vicinity of a THz metasurface, the non-radiative absorption losses of all meta-atoms are increased by an amount proportional to the real part of the graphene conductivity of Eq. (1). By increasing the graphene carrier density with a gate voltage, the metasurface quality factor can then be decreased in a controllable fashion, leading to a proportional reduction in transmission and reflection, as well as in the phase excursion across the resonance of each meta-atom.

This idea was initially demonstrated in Ref. [69] with a transmissive metasurface consisting of a periodic array of identical Au elements (hexagonal or double-split circular rings). The graphene sheet was deposited directly on the meta-atom array and gated across a thin polyimide layer with wire-shaped electrodes. Correspondingly, a transmission amplitude modulation of up to 47% was measured, accompanied by a maximum phase change of 32° at 0.65 THz. In a subsequent report [70], a larger phase modulation of over 90° was demonstrated at microwave frequencies with a similar configuration (consisting of an array of square split-ring resonators tuned with a double-graphene capacitor). While these devices are promising for switching applications, their use for wavefront shaping is hindered by their limited phase tunability. In fact, because of their transmissive single-resonance nature, the maximum phase modulation achievable with these metasurfaces is fundamentally limited to less than π, as shown by the Smith chart of Fig. 2(b).

By the same argument, the full 2π phase range becomes accessible if a back reflector is introduced in the metasurface substrate to produce the single-port reflective configuration of Fig. 2(a). This approach was demonstrated in Ref. [60] [Fig. 3], with meta-atoms consisting of Al rectangular mesas supported by a polymer (SU-8) spacer on an Al film reflector. This geometry supports magnetic dipolar resonances (near 0.3 THz) associated with a circulating AC current between each mesa and the metallic ground plane. Active tunability is again enabled by a continuous graphene sheet deposited over the meta-atom array and gated across a top ion-gel layer. If the graphene free-carrier absorption is sufficiently small (i.e., for sufficiently low gate voltages V_G), the Al meta-atoms are over-coupled to free-space radiation: correspondingly, the reflection amplitude decreases with increasing V_G [Fig. 3(a)], and the phase spans the full 2π range across the resonance [Fig. 3(b)]. At larger gate voltages, the meta-atoms become under-coupled, so that the reflection amplitude increases with increasing V_G [Fig. 3(c)] while the phase excursion is limited to less than π [Fig. 3(d)]. This behavior is fully consistent with the picture of Fig. 2(a), since for the meta-atoms of Fig. 3 the nonradiative decay rate Γ_{nr} is proportional to V_G. By using mesas of different dimensions gated with different voltages across the array, various wavefront shaping functionalities could then be implemented. Similar results have also been reported at

Optical Materials EXPRESS

mid-infrared wavelengths [71], where varying the graphene carrier density mostly modulates the refractive index leading to a shift in the meta-atom resonance frequency.

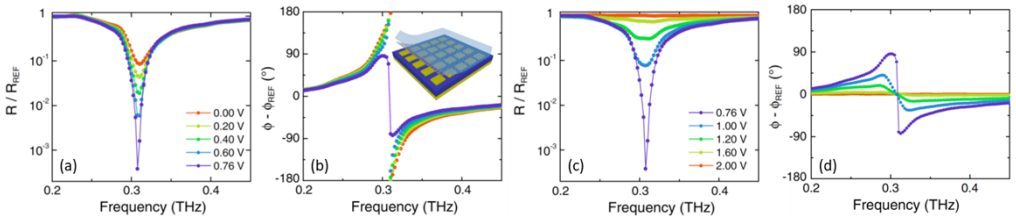

Fig. 3. Reflective metallic metasurface with a graphene tuning element. (a), (b) Measured frequency variations of the reflectivity (a) and reflection phase (b) across the meta-atom resonance, for different values of the graphene Fermi energy E_F for which the meta-atoms are over-coupled to free-space radiation. (c), (d) Same as (a) and (b), respectively, for different values of E_F for which the meta-atoms are under-coupled. The schematic device geometry is shown in the inset of (b). Reproduced under the terms of Creative Commons Attribution 3.0 License from Ref. 60.

Graphene sheets have also been integrated in metallic THz metasurfaces based on the Pancharatnam-Berry (PB) phase [72–74]. In this configuration, the meta-atoms are anisotropic scattering elements with slow and fast axes rotated by an angle θ relative to a fixed *x*-*y* reference frame [Fig. 4(a)]. If the incident light is left-circularly-polarized (LCP), an abrupt local phase shift of 2θ is introduced in the right-circularly-polarized (RCP) component of the transmitted wave (and vice versa for RCP illumination) [58]. In Ref. [72], the metallic metasurface consists of a Au film with U-shaped apertures, coated with a graphene sheet with a top ion-gel gate dielectric. In the configuration of Fig. 4(a), the rotation angle θ varies in equal steps δθ between neighboring meta-atoms separated by an equal distance δ*x* along the *x* direction. As a result, circularly polarized incident light acquires a linear phase profile $\phi(x) = \xi x = 2x\delta\theta/\delta x$ upon cross-polarized transmission, and therefore is deflected by a finite angle $\alpha_t = \arcsin(c\xi/2\pi\nu)$ on the *x*-*z* plane (anomalous refraction). This expectation is confirmed by the data of Fig. 4(b), showing the measured RCP transmitted intensity versus angle of refraction under normal-incidence LCP illumination at frequency ν = 1.15 THz. The role of the graphene sheet in this case is simply to vary the transmission by introducing a gate-tunable absorption loss across the full device bandwidth [Fig. 4(c)].

In general, in a PB metasurface, the local phase shift is the sum of the PB (geometric) phase, which only depends on the meta-atom orientation, plus the resonance contribution of the meta-atom, which also depends on its detailed geometry. In the device of Fig. 4(a), all meta-atoms have the same size and shape, and as a result the latter contribution is uniform across the entire array. In subsequent work [73], a PB metasurface was developed where the neighboring meta-atoms (rectangular apertures in a Au film) have different dimensions as well as different orientations [Fig. 4(d)]. By varying the gate voltage across an overlaying sheet of graphene, the resonance phase contribution of each meta-atom could therefore be tuned [through the Fermi-energy dependence of the conductivity of Eq. (1)] by a different amount for different meta-atoms. As a result, the metasurface phase profile could be reconfigured dynamically. In the device of Fig. 4(d), the meta-atoms were designed to produce the transmission phase profile of a lens, i.e., $\phi(x,y) = 2\pi\nu\left(f - \sqrt{f^2 + x^2 + y^2}\right)/c$, with different focal lengths f for different gate voltages. Correspondingly, a metalens with actively tunable focal length from 10.46 to 12.24 mm was experimentally demonstrated at ν = 0.75 THz [Figs. 4(e) and 4(f)].

More recently, the same general idea has also been explored in graphene-loaded non-BP metallic metasurfaces, where wavefront shaping relies entirely on the resonance phase distribution [75–77].

Optical Materials EXPRESS

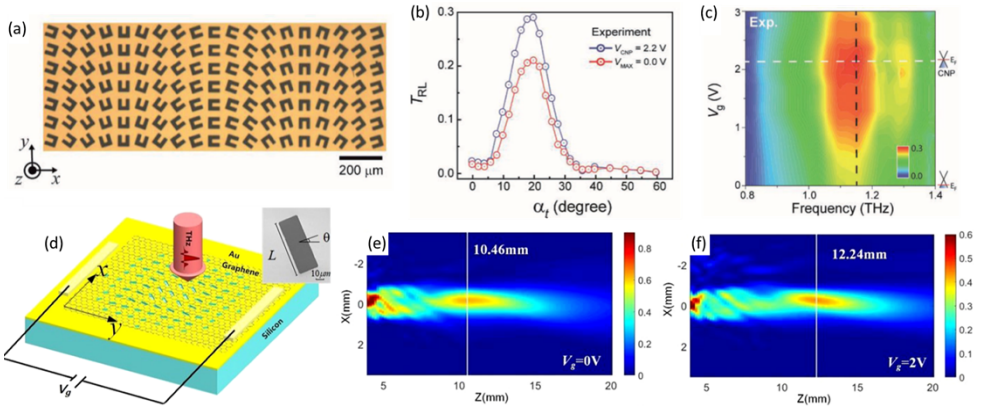

Fig. 4. Pancharatnam-Berry (PB) metallic metasurfaces with a graphene tuning element. (a) Optical microscope image of an array of U-shaped apertures in a Au film, with different orientations designed to produce a linear PB phase profile. (b) Measured cross-polarized transmitted light intensity through the metasurface of (a) (loaded with an overlaying sheet of graphene) versus transmission angle under normal-incidence LCP illumination at 1.15 THz. (c) Transmission spectrum of the same device at the angle of peak refraction for different values of the graphene gate voltage. (d) Schematic illustration of a graphene-loaded PB metasurface consisting of rectangular apertures in a Au film, with different orientations and dimensions designed to produce a lens phase profile. (e), (f) Cross-polarized transmitted light intensity through the metasurface of (d) as a function of position on the *x*-*z* plane under normal-incidence LCP illumination at 0.75 THz, for two different values of the graphene gate voltage V_g. (a)-(c) reproduced with permission from Ref. [72], Copyright (2018), WILEY-VCH Verlag GmbH & Co. KGaA, Weinheim. (d)-(f) reproduced from Ref. [73], Copyright (2018), Optica Publishing Group.

Specifically, these works employ meta-atoms with a sufficiently large number of geometrical parameters (e.g., C-shaped apertures in a Au film [75,76] or coupled Au stripes [77]), so that an array can be designed that produces a lens phase profile with different focal lengths for different Fermi energies of the adjacent graphene sheet. Actively tunable metalenses (for linearly polarized incident light) were again reported with this approach at frequencies $\lesssim$ 1 THz.

3.2. *Graphene plasmonic phase-gradient metasurfaces*

As the incident frequency ν is increased into the multiple-THz range, the graphene free-carrier absorption becomes progressively weaker following the characteristic ν^{-2} dependence that can be derived from Eq. (1). Correspondingly, strong GPP resonances emerge in suitably shaped graphene meta-atoms. Therefore, tunable metasurfaces operating in this frequency range can be developed based on such resonances. This idea has been explored in several theoretical studies in the past few years, which are reviewed in this section, although an experimental demonstration is yet to be reported. Most of these studies have focused on ribbon-shaped meta-atoms, which are well established and easy to gate as mentioned above. At the same time, it should be noted that the resulting metasurfaces are intrinsically limited to wavefront shaping on the plane perpendicular to the ribbons, and for light linearly polarized on the same plane.

Initial work considered an array of independently gated free-standing graphene nanoribbons [78]. With this arrangement, the authors demonstrated numerically gate-tunable anomalous refraction and focusing at mid-infrared wavelengths. Importantly, however, the phase tuning range in this transmissive geometry is again limited to less than π [see Fig. 2(b)]. As a result, the metasurface can only implement a limited portion of any desired phase profile that extends

Optical Materials EXPRESS

beyond the π range. This requirement restricts the lateral size of the metasurface to values on the order of a few wavelengths, depending on the desired phase gradients. Correspondingly, the device efficiency is degraded by aperture diffraction effects, and applications involving large wavefront distortions (e.g., steering by large angles) cannot be realized.

This limitation can be addressed using a reflective metasurface geometry, and substantial work [79–85] has focused on the architecture shown in Fig. 5(a) [80], consisting of an array of graphene ribbons on a dielectric cavity of suitable sub-wavelength thickness with a metallic back reflector. From Eq. (4), the ribbon plasmonic resonance can be tuned by varying the gate voltage V_G and the ribbon width w. Therefore, both parameters can be used to control the reflection phase of each meta-atom at any given frequency around the resonance. Figure 5(b) shows the width dependence of the reflection amplitude and phase at 12.32 THz, computed in Ref. [80] for a graphene ribbon with sufficiently large Fermi energy and mobility (0.64 eV and 10,000-cm^2/V/s, respectively) to enable a near-2π phase coverage. In the same work, the authors designed several metasurfaces, each consisting of many ribbons of different widths, to implement various functionalities such as anomalous reflection with >74% reflectivity, light focusing [Fig. 5(c)], and non-diffracting Airy beam formation. Because all the ribbons in these devices are gated at the same voltage, active tunability is mostly restricted to controlling the reflected light intensity, as illustrated in Figs. 5(c) and 5(d) for the metalens configuration.

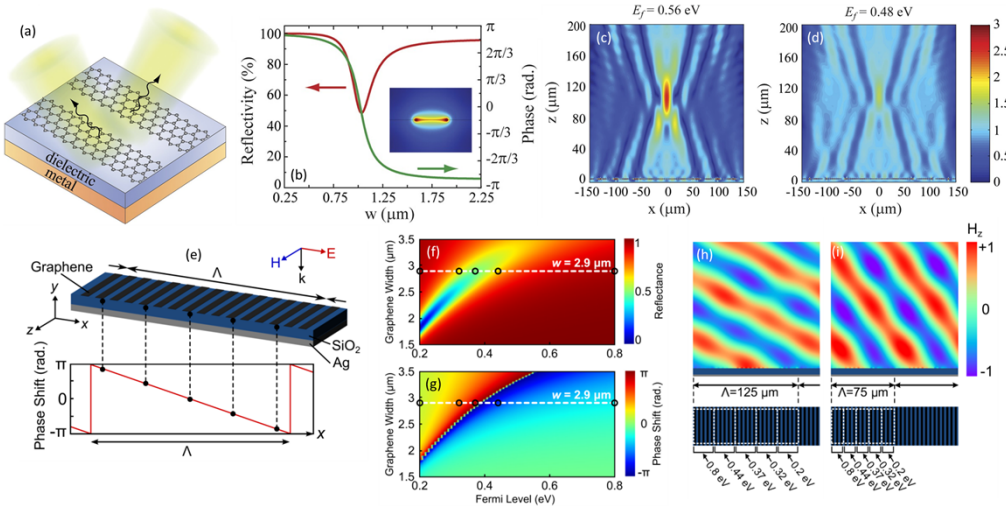

Fig. 5. Reflective metasurfaces based on graphene plasmonic ribbons. (a) Basic device geometry. (b) Reflectivity and reflection phase at 12.32 THz versus ribbon width w for fixed Fermi energy (0.64 eV). The inset shows the optical-field-intensity distribution on the ribbon cross-section at resonance for w = 1.035 μm. (c), (d) Calculated optical-field-intensity distribution on the plane perpendicular to the ribbons for a metasurface based on the meta-atoms of (b), with widths selected to produce the phase profile of a cylindrical lens. The Fermi energy of all ribbons is 0.56 eV in (c) and 0.48 eV in (d). (e) Schematic illustration of a device consisting of ribbons of equal width (2.9 μm) and different Fermi energies selected to produce a linear phase profile. (f), (g) Reflectivity and reflection phase at 5 THz versus ribbon width and Fermi energy. (h), (i) Calculated optical field distribution on the plane perpendicular to the ribbons for the device of (e)-(g), with different combinations of the ribbon Fermi energies (shown at the bottom of each panel) producing different phase slopes. (a)-(d) reproduced under the terms of Creative Commons Attribution 4.0 International License from Ref. 80. (e)-(i) reproduced with permission from Ref. 81, Copyright (2015), AIP Publishing.

Optical Materials EXPRESS

The phase profile imparted by the metasurface on the incident light can be tailored actively (and essentially at will) if the individual ribbons are gated separately with different voltages. In practice, this approach requires a large but realistic number (several 10s) of electrical control signals, which can be applied on a printed circuit board (a similar setup has been reported recently with a near-infrared metallic metasurface based on transparent conducting oxides [86]). Figures 5(e)-(i) illustrate a device designed to provide a linear phase profile with actively tunable slope (i.e., anomalous reflection at variable angles) at 5 THz [81]. All the ribbons have the same width of 2.9 μm, and their reflection phase can be varied across 2π by varying the Fermi energy between 0.2 and 0.8 eV (assuming a relaxation lifetime τ of 1 ps) [Fig. 5(g)]. Numerical simulations for different gating configurations confirm the expected tunable beam steering operation with 60% reflection efficiency up to 53° steering angle [Figs. 5(h) and 5(i)]. Similar structures with similar assumptions on the relevant materials properties have also been designed to demonstrate cylindrical metalenses with actively tunable focal length [82,83] (e.g., from 100 to 300 μm at 5 THz in Ref. 82) and even cloaking of triangular bumps on a flat surface [84].

Graphene plasmonic resonators have also been used in PB metasurfaces, to enable full-2π phase coverage in transmission [Fig. 6(a)] [87] and to design actively tunable metalenses [88,89]. The work of Ref. 88 [Fig. 6(b)] employs rectangular apertures of different sizes and orientations in a continuous sheet of graphene (again on a reflective substrate). Gate tuning of the focal length f is then achieved by combining the PB and resonant phase contributions to produce the lens phase profile, similar to the approach of Ref. 73 reviewed in Figs. 4(d)-(f). The resulting tuning range is somewhat limited, with f varying from 136 to 180 μm at 5 THz while the focusing efficiency decreases from 60% to 15%. A higher efficiency of over 70% for a tuning range of 73 μm at 4.5 THz was subsequently computed for a similar structure based on elliptical apertures [89]. Importantly, even though these works only consider cylindrical metalenses (with focusing restricted on a single plane), the same approach can in principle be extended to full three-dimensional focusing, unlike all designs based on the ribbon geometry.

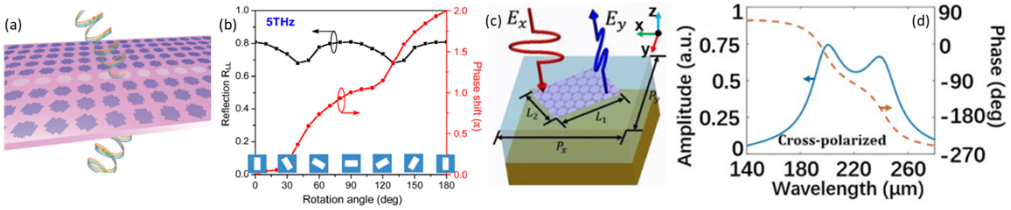

Fig. 6. Graphene plasmonic metasurfaces based on alternative meta-atom geometries. (a) Schematic illustration of a transmissive PB metasurface based on graphene plasmonic nanocrosses. (b) Reflectivity and reflection phase shift under LCP illumination at 5 THz versus meta-atom rotation angle, for a reflective PB metasurface based on rectangular apertures in a graphene sheet. The dips observed in these traces can be attributed to coupling of the incident light to the aperture resonances. (c) Meta-atoms consisting of rectangular graphene patches rotated by 45° relative to the periodicity axes. (d) Cross-polarized reflectivity and reflection phase versus wavelength for a periodic array of the structure of (c). (a) reproduced with permission from Ref. [87], Copyright (2015), WILEY-VCH Verlag GmbH & Co. KGaA, Weinheim. (b) reproduced from Ref. [88], Copyright (2018), Optica Publishing Group. (c), (d) reproduced from Ref. [90], Copyright (2017), Optica Publishing Group.

In a different approach [90], the meta-atoms consist of rectangular patches distributed periodically along the x and y directions and oriented at 45° [Fig. 6(c)]. The patch dimensions are selected to introduce a π reflection-phase difference between the incident polarization components along the two axes of the rectangle. As a result, incident light with x-polarization is

Optical Materials EXPRESS

cross-polarized upon reflection, while the overall reflection phase is geometrically tunable across 2π [Fig. 6(d)]. In Ref. 90, various device operations based on such meta-atoms are presented, including polarization switching, anomalous reflection, and light focusing and defocusing. Additional reflective configurations from the recent literature include multiple patches per unit cell to allow for geometrically tunable focusing on the same spot at different wavelengths [91] and tapered ribbons to reflect different wavelengths along widely different directions [92]. The use of different dielectric-spacer thicknesses in different meta-atoms has also been explored as an additional degree of freedom for tuning the reflection phase [93]. Finally, devices consisting of multiple meta-atom arrays stacked on top of one another have also been investigated to create more functionality [94–96], at the expense however of increased fabrication complexity.

All the numerical studies reviewed so far in this section assume extremely high carrier mobilities μ (typically 10,000 $cm^2/V/s$), often combined with exceedingly large Fermi energies E_F (up to 1 eV [82,87,88,92,96]). These assumptions are essential to ensure that the relaxation time τ of Eq. (2) is sufficiently long, so that the over-coupling condition $\Gamma_{rad} > \Gamma_{nr} = 1/\tau$ is satisfied for the meta-atom plasmonic resonances [see Fig. 2(a)]. Such mobility values are indeed accessible with exfoliated graphene, at least at more moderate carrier densities. Unfortunately, however, the resulting samples are too small for the envisioned device applications, as mentioned above. This limitation likely plays a key role in the lack of experimental progress with these devices so far. More recently, a new metasurface design has been proposed that can support over-coupled resonances at mobilities accessible with large-area CVD samples on Si/SiO_2 (~ 2,000 $cm^2/V/s$) for reasonable Fermi levels below 0.6 eV [61].

This design consists of the periodic repetition of identical meta-units, each comprising two double-layer graphene ribbons of different widths interspersed with Au rectangular antennas [Fig. 7(a)]. Once again, the ribbons are supported by a $Au/Si/SiO_2$ cavity. As illustrated in Fig. 2(d), Au antennas can effectively funnel light in and out of ribbon GPPs, and correspondingly enhance their radiative decay rate Γ_{rad}. As a result, the over-coupling condition can be satisfied even for the relatively short relaxation times τ of CVD graphene ($\lesssim$ 100 fs). The use of two ribbons per unit cell further allows to increase the phase tuning range by optimizing the fill factor. Figures 7(b) and 7(c) show the reflection magnitude $|r|^2$ and phase ϕ_r of each meta-atom of this device at 3 THz, computed as a function of the Fermi energies $\tilde{E}_{F1}$ and $\tilde{E}_{F2}$ of the two ribbons for μ = 2,000 $cm^2/V/s$. Two points of maximum absorption can be identified in Fig. 7(b), around which ϕ_r spans the full 2π interval as shown in Fig. 7(c). The dashed lines in both color maps show the combinations of Fermi energies that produce each value of ϕ_r from 0 to 2π with the

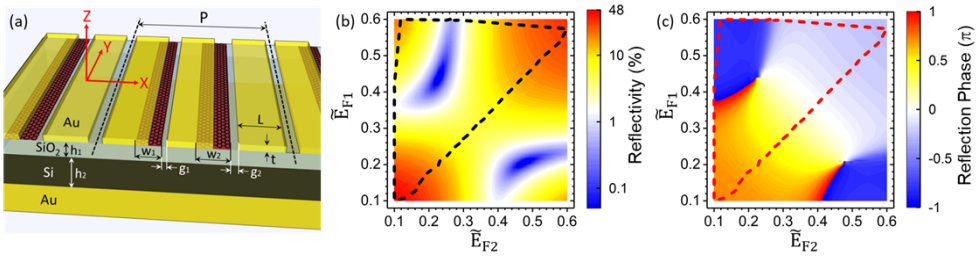

Fig. 7. Reflective metasurface based on graphene plasmonic ribbons coupled to Au rectangular antennas. (a) Schematic device geometry. (b), (c) Reflectivity $|r|^2$ (b) and reflection phase ϕ_r (c) at 3 THz versus effective Fermi energies $\tilde{\mathbf{E}}_{\mathbf{F1}}$ and $\tilde{\mathbf{E}}_{\mathbf{F2}}$ of the two double-layer graphene ribbons for μ = 2,000 $cm^2/V/s$. The dashed lines show all the combinations of values of $\tilde{\mathbf{E}}_{\mathbf{F1}}$ and $\tilde{\mathbf{E}}_{\mathbf{F2}}$ for which ϕ_r covers the full range from 0 to 2π for the largest possible $|r|^2$. Reproduced from Ref. 61, Copyright (2021), Optica Publishing Group.

Optical Materials EXPRESS

largest possible $|r|^2$. By separately controlling the gate voltages of all the ribbons according to these prescriptions, tunable beam steering (up to a maximum angle of over 60°) and focusing (with variable focal length between 0.9 and 2.2 mm) were demonstrated numerically in Ref. [61], with reasonable efficiencies in the 21-35% range.

4. Graphene THz light-emitting metasurfaces

Graphene is also a promising material system for device applications in THz optoelectronics [15,97], by virtue of several distinctive properties including its gapless and linear electronic energy dispersion, ultrahigh intrinsic mobility, and long-wavelength plasmonic resonances. In this context, the use of metasurfaces is generally attractive as a way to enhance the light-matter interaction strength, which is otherwise limited by the ultrasmall thickness of monolayer graphene. For example, graphene ribbon arrays have been used to increase contrast in THz modulators [65,66] and photovoltage in THz photodetectors based on the photo-thermoelectric effect [98]. By the reverse process, if GPPs are excited in a metasurface (e.g., by thermal or electrical means), light emission at the plasmonic resonance frequency of the meta-atoms can be produced. This idea has been demonstrated at mid-infrared and THz wavelengths in Refs. [99] and [100], respectively, with GPPs excited by heating the sample substrate [99] and through the injection of electrical current [100].

The latter approach is described in Fig. 8. The metasurfaces in these devices consist of multiple CVD graphene ribbons connected between the source and drain contacts, with perpendicular "bridge" sections between neighboring ribbons used to minimize the impact of cracks on the overall current flow [Fig. 8(a)]. The device operation relies on the generation of hot carriers in the ribbons under direct current injection, and their subsequent energy relaxation through the excitation of GPPs. Narrowband free-space THz radiation is then emitted by the resulting collective oscillations of the graphene electron gas. Figure 8(b) shows emission spectra measured with a recent (unpublished) device based on this approach, consisting of an array of 800-nm-wide ribbons with an active graphene area of about 0.1 mm^2 on a Si/SiO_2 substrate. The expected gate tunability of the emission frequency is clearly illustrated by these data, in good agreement with the expression of Eq. (4) for the GPP resonance frequency ν_1 [see figure inset]. As shown in Fig. 8(c), THz light emission in this device is observed up to a maximum substrate temperature T_{base} of 240 K, and the highest recorded output power P_{out} is 24 nW for an input electrical power P_{in} (related to the injection current) of 1 W at $T_{base} = 80$ K. These data represent a substantial improvement over the results reported in Ref. [100] (where P_{out} at the same temperature was limited to a maximum value of 2.8 nW), due to the larger active area and improved materials quality of the present sample.

The underlying radiation mechanism of these devices can be described as thermal emission resonantly enhanced by the excitation of GPPs [101]. From Kirchhoff's law of thermal radiation, the output power spectrum is then given by Planck's formula for blackbody emission multiplied by the ribbon absorption efficiency η [102]. The latter parameter (universally defined as the ratio between absorption cross-section and physical surface area) can be well above one at frequencies near an absorption resonance. In the devices of Ref. [100] and Figs. 8(a)-(c), however, η is limited to a few % due to the under-coupled nature of GPPs in CVD graphene ribbons (see section 2.4), as well as the presence of a transmissive channel in the Si/SiO_2 substrate [101]. Significantly higher output power can therefore be expected in device structures designed to enable critical coupling and perfect absorption at the mobility values of CVD graphene.

A suitable design, based on the same prescriptions of the metasurface of Fig. 7, is shown in Fig. 8(d) [101]. In this device, the GPP radiative decay rate Γ_{rad} is maximized by coupling each ribbon to two neighboring Au patch antennas, following the general behavior illustrated in Fig. 2(d). Additionally, perfect absorption can be achieved with the supporting $Au/Si/SiO_2$ vertical cavity, where the back mirror is used to block transmission of the incident light and at

Optical Materials EXPRESS

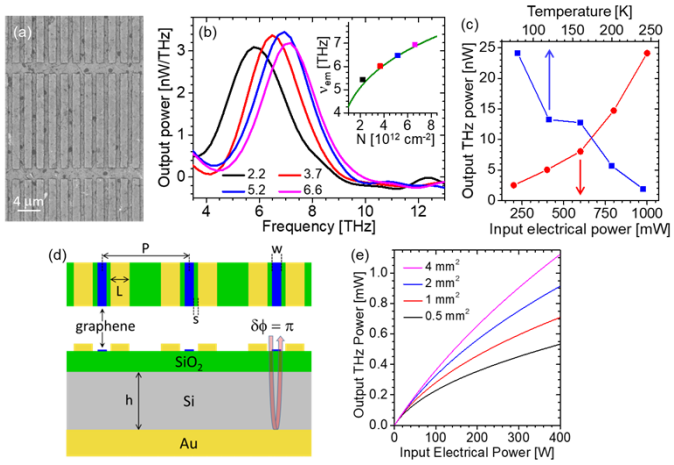

Fig. 8. Graphene THz light-emitting metasurfaces. (a) Top-view scanning electron microscopy (SEM) image of an experimental sample. (b) Measured emission spectra for $T_{base} = 80$ K, $P_{in} = 0.2$ W, and different values of carrier density N (listed in the legend in units of 10^{12} cm^{-2}). Each trace is normalized to the spectrum measured under the same conditions at charge neutrality. Inset: peak emission frequencies extracted from the spectra of (a) (symbols) and calculated plasmonic resonance frequency versus carrier density from Eq. (4) (solid line). (c) Plasmonic THz output power P_{out} estimated from the measured emission spectra using the procedure described in Ref. [100], plotted versus input electrical power P_{in} for $T_{base} = 80$ K (bottom axis) and versus substrate base temperature T_{base} for $P_{in} = 1$ W (top axis). The carrier density is $N = 3.7 \times 10^{12}$ cm^{-2}. (d) Schematic device structure designed to maximize the plasmonic radiation output by promoting critical coupling. (e) Calculated room-temperature THz output power of the same device (assuming a mobility μ of 2000 cm^2/V) versus input electrical power for different values of the graphene surface area. (d), (e) reproduced with permission from Ref. [101], Copyright (2020), AIP Publishing.

the same time suppress reflection by interference (with the proper choice of graphene-mirror separation) [62,63]. With this approach, detailed calculations show that large output power levels approaching 1 mW can be achieved at room temperature with device active areas of a few mm^2 and input electrical powers of a few 100 W [Fig. 8(e)] [101]. The corresponding electrical power densities of a few 100 W/mm^2 are large but experimentally accessible and well below the reported graphene damage threshold [103].

Further improvements in radiative efficiency could be obtained through the injection of minority carriers in the nanoribbons (e.g., electrons in *p*-doped samples or vice versa). Under these conditions, GPP emission via carrier recombination becomes extremely efficient [41,42,104], so that a much higher density of plasmonic excitations can be established compared to the thermal emitters of Fig. 8. Various configurations could be used to produce the required nonequilibrium carrier distributions, including optical pumping and electrical injection across a forward-biased *p*-*n* junction in a double-gated device. These ideas have already been investigated extensively towards the development of graphene THz lasers [105–108], although it is still unclear whether optical gain can indeed be established in graphene active media. In contrast, the devices of Fig. 8(d) do not require population inversion, but would still highly benefit from the enhanced GPP excitation efficiency under nonequilibrium carrier injection.

Optical Materials EXPRESS

5. Conclusion and outlook

We have reviewed recent work on graphene THz metasurfaces, focused on three general classes of devices: (1) low-frequency ($\lesssim$ 1 THz) wavefront-shaping metasurfaces based on metallic meta-atoms with a continuous sheet of graphene used as an actively tunable loss element; (2) tunable wavefront-shaping metasurfaces operating at multiple-THz frequencies based on graphene plasmonic meta-atoms; (3) THz light-emitting metasurfaces based on graphene plasmonic ribbons. Extensive theoretical work has produced several design strategies for the development of multifunctional graphene metasurfaces, although experimental progress so far has been limited to low-frequency devices based on graphene-tunable metallic meta-atoms. The initial measurement of THz light emission from graphene ribbons has also been reported, albeit only at low temperatures and with limited wall-plug efficiency.

Going forward, we expect that the experimental demonstration of various THz wavefront-shaping operations with graphene plasmonic meta-atoms is fully within reach. As described in detail above, the key challenge in this context (i.e., the limited radiative coupling of GPPs) can be effectively addressed by combining the graphene plasmonic resonators with specially designed optical elements. The use of recently developed growth and transfer techniques to improve the mobility of large-area CVD graphene samples [39,40] is also likely to play an important role in the further development of these devices. From a practical standpoint, the same devices will also benefit from a robust ion-gel materials technology for the FET gate dielectric (e.g., as in Ref. [30]), to allow for active gating and dynamic tuning at reasonably low voltages. With the same prescriptions, possibly combined with suitable schemes for nonequilibrium carrier injection, we also envision that THz light-emitting metasurfaces can reach near-mW output power levels at room temperature. The resulting devices could then compete favorably with existing technologies for THz light emission [23,24], particularly in light of their compactness and ease of integration.

From a design perspective, an important endeavor that is still largely unexplored with graphene metasurfaces is dispersion engineering, e.g., to enable broadband achromatic response or to allow for tailored frequency-selective operation depending on the desired application. Additionally, most structures considered so far are based on quasi-1D ribbon-shaped meta-atoms, and therefore can only control the phase profile in one direction and for one polarization. Ultimately, polarization-independent wavefront shaping in all directions would also be required to extend the range of possible applications. The key challenge in this respect is related to the need to individually control the gate voltages of many isolated 2D meta-atoms, which will likely require integrating the metasurfaces with complex microelectronic circuits in the supporting Si chip. Altogether, the resulting device technology can be expected to have a transformative impact on a wide range of THz imaging and sensing applications, e.g., for developing novel cameras and spectrometers with enhanced miniaturization and functionality. Furthermore, it may play an enabling role in future THz wireless communications beyond 5 G, e.g., for dynamically reconfigurable routing and multiplexing.

Funding. National Science Foundation (ECCS-2111160).

Acknowledgments. The FDTD simulations were performed using the Shared Computing Cluster facility at Boston University.

Disclosures. The authors declare no conflicts of interest.

Data availability. Data underlying the results presented in this paper are not publicly available at this time but may be obtained from the authors upon reasonable request.

References

1. N. Yu and F. Capasso, "Flat optics with designer metasurfaces," Nat. Mater. **13**(2), 139–150 (2014).
2. F. Ding, A. Pors, and S. I. Bozhevolnyi, "Gradient metasurfaces: a review of fundamentals and applications," Rep. Prog. Phys. **81**(2), 026401 (2018).
3. S. M. Kamali, E. Arbabi, A. Arbabi, and A. Faraon, "A review of dielectric optical metasurfaces for wavefront control," Nanophotonics **7**(6), 1041–1068 (2018).

Optical Materials EXPRESS

4. L. C. Kogos and R. Paiella, "Light emission near a gradient metasurface," ACS Photonics **3**(2), 243–248 (2016).
5. S. Liu, A. Vaskin, S. Addamane, B. Leung, M.-C. Tsai, Y. Yang, P. P. Vabishchevich, G. A. Keeler, G. Wang, X. He, Y. Kim, N. F. Hartmann, H. Htoon, S. K. Doorn, M. Zilk, T. Pertsch, G. Balakrishnan, M. B. Sinclair, I. Staude, and I. Brener, "Light-emitting metasurfaces: simultaneous control of spontaneous emission and far-field radiation," Nano Lett. **18**(11), 6906–6914 (2018).
6. A. Vaskin, R. Kolkowski, A. F. Koenderink, and I. Staude, "Light-emitting metasurfaces," Nanophotonics **8**(7), 1151–1198 (2019).
7. X. Wang, Y. Li, R. Toufanian, L. C. Kogos, A. Dennis, and R. Paiella, "Geometrically-tunable beamed light emission from a quantum-dot ensemble near a gradient metasurface," Adv. Opt. Mater. **8**(8), 1901951 (2020).
8. P. P. Iyer, R. A. DeCrescent, Y. Mohtashami, G. Lheureux, N. A. Butakov, A. Alhassan, C. Weisbuch, S. Nakamura, S. P. DenBaars, and J. A. Schuller, "Unidirectional luminescence from InGaN/GaN quantum-well metasurfaces," Nat. Photonics **14**(9), 543–548 (2020).
9. A. N. Grigorenko, M. Polini, and K. S. Novoselov, "Graphene plasmonics," Nat. Photonics **6**(11), 749–758 (2012).
10. T. Low and P. Avouris, "Graphene plasmonics for terahertz to mid-infrared applications," ACS Nano **8**(2), 1086–1101 (2014).
11. F. J. García de Abajo, "Graphene plasmonics: challenges and opportunities," ACS Photonics **1**(3), 135–152 (2014).
12. S. Xiao, X. Zhu, B. Li, and N. A. Mortensen, "Graphene-plasmon polaritons: from fundamental properties to potential applications," Front. Phys. **11**(2), 117801 (2016).
13. Q. Guo, C. Li, B. Deng, S. Yuan, F. Guinea, and F. Xia, "Infrared nanophotonics based on graphene plasmonics," ACS Photonics **4**(12), 2989–2999 (2017).
14. J. Cheng, F. Fan, and S. Chang, "Recent progress on graphene-functionalized metasurfaces for tunable phase and polarization control," Nanomaterials **9**(3), 398 (2019).
15. Y. Li, K. Tantiwanichapan, A. K. Swan, and R. Paiella, "Graphene plasmonic devices for terahertz optoelectronics," Nanophotonics **9**(7), 1901–1920 (2020).
16. A. M. Shaltout, V. M. Shalaev, and M. L. Brongersma, "Spatiotemporal light control with active metasurfaces," Science **364**(6441), eaat3100 (2019).
17. X. Zhang, Z. Tian, W. Yue, J. Gu, S. Zhang, J. Han, and W. Zhang, "Broadband terahertz wave deflection based on C-shape complex metamaterials with phase discontinuities," Adv. Mater. **25**(33), 4567–4572 (2013).
18. T. Niu, W. Withayachumnankul, B. S.-Y. Ung, H. Menekse, M. Bhaskaran, S. Sriram, and C. Fumeaux, "Experimental demonstration of reflectarray antennas at terahertz frequencies," Opt. Express **21**(3), 2875–2889 (2013).
19. Z. Ma, S. M. Hanham, P. Albella, B. Ng, H. T. Lu, Y. Gong, S. A. Maier, and M. Hong, "Terahertz all-dielectric magnetic mirror metasurfaces," ACS Photonics **3**(6), 1010–1018 (2016).
20. M. Liu, Q. Yang, A. A. Rifat, V. Raj, A. Komar, J. Han, M. Rahmani, H. T. Hattori, D. Neshev, D. A. Powell, and I. V. Shadrivov, "Deeply subwavelength metasurface resonators for terahertz wavefront manipulation," Adv. Opt. Mater. **7**(21), 1900736 (2019).
21. H. W. Tian, H. Y. Shen, X. G. Zhang, X. Li, W. X. Jiang, and T. J. Cui, "Terahertz metasurfaces: toward multifunctional and programmable wave manipulation," Front. Phys. **8**, 584077 (2020).
22. C. Chen, K. Kaj, X. Zhao, Y. Huang, R. D. Averitt, and X. Zhang, "On-demand terahertz surface wave generation with microelectromechanical-system-based metasurface," Optica **9**(1), 17–25 (2022).
23. D. M. Mittleman, "Frontiers in terahertz sources and plasmonics," Nat. Photonics **7**(9), 666–669 (2013).
24. G. Valušis, A. Lisauskas, H. Yuan, W. Knap, and H. G. Roskos, "Roadmap of terahertz imaging 2021," Sensors **21**(12), 4092–4142 (2021).
25. H. Elayan, O. Amin, B. Shihada, R. M. Shubair, and M.-S. Alouini, "Terahertz band: The last piece of RF spectrum puzzle for communication systems," IEEE Open J. Commun. Soc. **1**, 1–32 (2020).
26. G. W. Hanson, "Dyadic Green's functions and guided surface waves for a surface conductivity model of graphene," J. Appl. Phys. **103**(6), 064302 (2008).
27. M. Jablan, H. Buljan, and M. Soljačić, "Plasmonics in graphene at infrared frequencies," Phys. Rev. B **80**(24), 245435 (2009).
28. A. H. Castro Neto, F. Guinea, N. M. R. Peres, K. S. Novoselov, and A. K. Geim, "The electronic properties of graphene," Rev. Mod. Phys. **81**(1), 109–162 (2009).
29. P. Q. Liu, F. Valmorra, C. Maissen, and J. Faist, "Electrically tunable graphene anti-dot array terahertz plasmonic crystals exhibiting multi-band resonances," Optica **2**(2), 135–140 (2015).
30. L. Ju, B. Geng, J. Horng, C. Girit, M. Martin, Z. Hao, H. A. Bechtel, X. Liang, A. Zettl, Y. R. Shen, and F. Wang, "Graphene plasmonics for tunable terahertz metamaterials," Nat. Nanotechnol. **6**(10), 630–634 (2011).
31. D. Rodrigo, A. Tittl, O. Limaj, F. J. García de Abajo, V. Pruneri, and H. Altug, "Double-layer graphene for enhanced tunable infrared plasmonics," Light: Sci. Appl. **6**(6), e16277 (2017).
32. G. Li, V. Semenenko, V. Perebeinos, and P. Q. Liu, "Multilayer graphene terahertz plasmonic structures for enhanced frequency tuning range," ACS Photonics **6**(12), 3180–3185 (2019).
33. Y. Zhang, V. W. Brar, C. Girit, A. Zettl, and M. F. Crommie, "Origin of spatial charge inhomogeneity in graphene," *Nat. Phys.*. **5**(10), 722–726 (2009).
34. K. Tantiwanichapan, X. Wang, H. Durmaz, Y. Li, A. K. Swan, and R. Paiella, "Graphene terahertz plasmons: a combined transmission spectroscopy and Raman microscopy study," ACS Photonics **4**(8), 2011–2017 (2017).

Optical Materials EXPRESS

35. K. S. Novoselov, A. K. Geim, S. V. Morozov, D. Jiang, Y. Zhang, S. V. Dubonos, I. V. Grigorieva, and A. A. Firsov, "Electric field effect in atomically thin carbon films," Science **306**(5696), 666–669 (2004).
36. K. I. Bolotin, K. J. Sikes, J. Hone, H. L. Stormer, and P. Kim, "Temperature-dependent transport in suspended graphene," Phys. Rev. Lett. **101**(9), 096802 (2008).
37. L. Wang, I. Meric, P. Y. Huang, Q. Gao, Y. Gao, H. Tran, T. Taniguchi, K. Watanabe, L. M. Campos, D. A. Muller, J. Guo, P. Kim, J. Hone, K. L. Shepard, and C. R. Dean, "One-dimensional electrical contact to a two-dimensional material," Science **342**(6158), 614–617 (2013).
38. S. J. Kim, T. Choi, B. Lee, S. Lee, K. Choi, J. B. Park, J. M. Yoo, Y. S. Choi, J. Ryu, P. Kim, J. Hone, and B. H. Hong, "Ultraclean patterned transfer of single-layer graphene by recyclable pressure sensitive adhesive films," Nano Lett. **15**(5), 3236–3240 (2015).
39. W. S. Leong, H. Wang, J. Yeo, F. J. Martin-Martinez, A. Zubair, P.-C. Shen, Y. Mao, T. Palacios, M. J. Buehler, J.-Y. Hong, and J. Kong, "Paraffin-enabled graphene transfer," Nat. Commun. **10**(1), 867 (2019).
40. M. Wang, M. Huang, D. Luo, Y. Li, M. Choe, W. K. Seong, M. Kim, S. Jin, M. Wang, S. Chatterjee, Y. Kwon, Z. Lee, and R. S. Ruoff, "Single-crystal, large-area, fold-free monolayer graphene," Nature **596**(7873), 519–524 (2021).
41. F. Rana, J. H. Strait, H. Wang, and C. Manolatou, "Ultrafast carrier recombination and generation rates for plasmon emission and absorption in graphene," Phys. Rev. B **84**(4), 045437 (2011).
42. A. F. Page, F. Ballout, O. Hess, and J. M. Hamm, "Nonequilibrium plasmons with gain in graphene," Phys. Rev. B **91**(7), 075404 (2015).
43. J. Chen, M. Badioli, P. Alonso-González, S. Thongrattanasiri, F. Huth, J. Osmond, M. Spasenović, A. Centeno, A. Pesquera, P. Godignon, A. Z. Elorza, N. Camara, F. J. García de Abajo, R. Hillenbrand, and F. H. L. Koppens, "Optical nano-imaging of gate-tunable graphene plasmons," Nature **487**(7405), 77–81 (2012).
44. Z. Fei, A. S. Rodin, G. O. Andreev, W. Bao, A. S. McLeod, M. Wagner, L. M. Zhang, Z. Zhao, M. Thiemens, G. Dominguez, M. M. Fogler, A. H. Castro Neto, C. N. Lau, F. Keilmann, and D. N. Basov, "Gate-tuning of graphene plasmons revealed by infrared nano-imaging," Nature **487**(7405), 82–85 (2012).
45. X. Zhu, W. Yan, P. U. Jepsen, O. Hansen, N. A. Mortensen, and S. Xiao, "Experimental observation of plasmons in a graphene monolayer resting on a two-dimensional subwavelength silicon grating," Appl. Phys. Lett. **102**(13), 131101 (2013).
46. W. Gao, G. Shi, Z. Jin, J. Shu, Q. Zhang, R. Vajtai, P. M. Ajayan, J. Kono, and Q. Xu, "Excitation and active control of propagating surface plasmon polaritons in graphene," Nano Lett. **13**(8), 3698–3702 (2013).
47. K. Y. M. Yeung, J. Chee, H. Yoon, Y. Song, J. Kong, and D. Ham, "Far-infrared graphene plasmonic crystals for plasmonic band engineering," Nano Lett. **14**(5), 2479–2484 (2014).
48. J. Song, L. Zhang, Y. Xue, Q. Y. S. Wu, F. Xia, C. Zhang, Y.-L. Zhong, Y. Zhang, J. Teng, M. Premaratne, C.-W. Qiu, and Q. Bao, "Efficient excitation of multiple plasmonic modes on three-dimensional graphene: an unexplored dimension," ACS Photonics **3**(10), 1986–1992 (2016).
49. A. Y. Nikitin, T. Low, and L. Martin-Moreno, "Anomalous reflection phase of graphene plasmons and its influence on resonators," Phys. Rev. B **90**(4), 041407 (2014).
50. J. Christensen, A. Manjavacas, S. Thongrattanasiri, F. H. L. Koppens, and F. J. García de Abajo, "Graphene plasmon waveguiding and hybridization in individual and paired nanoribbons," ACS Nano **6**(1), 431–440 (2012).
51. H. Yan, T. Low, W. Zhu, Y. Wu, M. Freitag, X. Li, F. Guinea, P. Avouris, and F. Xia, "Damping pathways of mid-infrared plasmons in graphene nanostructures," Nat. Photonics **7**(5), 394–399 (2013).
52. V. W. Brar, M. S. Jang, M. Sherrott, J. J. Lopez, and H. A. Atwater, "Highly confined tunable mid-infrared plasmonics in graphene nanoresonators," Nano Lett. **13**(6), 2541–2547 (2013).
53. I. J. Luxmoore, C. H. Gan, P. Q. Liu, F. Valmorra, P. Li, J. Faist, and G. R. Nash, "Strong coupling in the far-infrared between graphene plasmons and the surface optical phonons of silicon dioxide," ACS Photonics **1**(11), 1151–1155 (2014).
54. H. Yan, X. Li, B. Chandra, G. Tulevski, Y. Wu, M. Freitag, W. Zhu, P. Avouris, and F. Xia, "Tunable infrared plasmonic devices using graphene/insulator stacks," Nat. Nanotechnol. **7**(5), 330–334 (2012).
55. X. Zhu, W. Wang, W. Yan, M. B. Larsen, P. Bøggild, T. G. Pedersen, S. Xiao, J. Zi, and N. A. Mortensen, "Plasmon–phonon coupling in large-area graphene dot and antidot arrays fabricated by nanosphere lithography," Nano Lett. **14**(5), 2907–2913 (2014).
56. Q. Guo, R. Yu, C. Li, S. Yuan, B. Deng, F. J. García de Abajo, and F. Xia, "Efficient electrical detection of mid-infrared graphene plasmons at room temperature," Nat. Mater. **17**(11), 986–992 (2018).
57. Z. Fang, S. Thongrattanasiri, A. Schlather, Z. Liu, L. Ma, Y. Wang, P. M. Ajayan, P. Nordlander, N. J. Halas, and F. J. García de Abajo, "Gated tunability and hybridization of localized plasmons in nanostructured graphene," ACS Nano **7**(3), 2388–2395 (2013).
58. M. V. Berry, "The adiabatic phase and Pancharatnam's phase for polarized light," J. Mod. Opt. **34**(11), 1401–1407 (1987).
59. S. Fan, W. Suh, and J. D. Joannopoulos, "Temporal coupled-mode theory for the Fano resonance in optical resonators," J. Opt. Soc. Am. A **20**(3), 569 (2003).
60. Z. Miao, Q. Wu, X. Li, Q. He, K. Ding, Z. An, Y. Zhang, and L. Zhou, "Widely tunable terahertz phase modulation with gate-controlled graphene metasurfaces," Phys. Rev. X **5**(4), 041027 (2015).

Optical Materials EXPRESS

61. Y. Li and R. Paiella, "Tunable terahertz metasurface platform based on CVD graphene plasmonics," Opt. Express **29**(24), 40594–40605 (2021).
62. S. Thongrattanasiri, F. H. L. Koppens, and F. J. García de Abajo, "Complete optical absorption in periodically patterned graphene," Phys. Rev. Lett. **108**(4), 047401 (2012).
63. R. Alaee, M. Farhat, C. Rockstuhl, and F. Lederer, "A perfect absorber made of a graphene micro-ribbon metamaterial," Opt. Express **20**(27), 28017–28024 (2012).
64. Y. Yao, R. Shankar, M. A. Kats, Y. Song, J. Kong, M. Loncar, and F. Capasso, "Electrically tunable metasurface perfect absorbers for ultrathin midinfrared optical modulators," Nano Lett. **14**(11), 6526–6532 (2014).
65. M. M. Jadidi, A. B. Sushkov, R. L. Myers-Ward, A. K. Boyd, K. M. Daniels, D. K. Gaskill, M. S. Fuhrer, H. D. Drew, and T. E. Murphy, "Tunable terahertz hybrid metal-graphene plasmons," Nano Lett. **15**(10), 7099–7104 (2015).
66. P. Q. Liu, I. J. Luxmoore, S. A. Mikhailov, N. A. Savostianova, F. Valmorra, J. Faist, and G. R. Nash, "Highly tunable hybrid metamaterials employing split-ring resonators strongly coupled to graphene surface plasmons," Nat. Commun. **6**(1), 8969 (2015).
67. S. Kim, M. S. Jang, V. W. Brar, K. W. Mauser, L. Kim, and H. A. Atwater, "Electronically tunable perfect absorption in graphene," Nano Lett. **18**(2), 971–979 (2018).
68. S. Han, S. Kim, S. Kim, T. Low, V. W. Brar, and M. S. Jang, "Complete complex amplitude modulation with electronically tunable graphene plasmonic metamolecules," ACS Nano **14**(1), 1166–1175 (2020).
69. S. H. Lee, M. Choi, T. T. Kim, S. Lee, M. Liu, X. Yin, H. K. Choi, S. S. Lee, C. G. Choi, S. Y. Choi, X. Zhang, and B. Min, "Switching terahertz waves with gate-controlled active graphene metamaterials," Nat. Mater. **11**(11), 936–941 (2012).
70. O. Balci, N. Kakenov, E. Karademir, S. Balci, S. Cakmakyapan, E. O. Polat, H. Caglayan, E. Özbay, and C. Kocabas, "Electrically switchable metadevices via graphene," Sci. Adv. **4**(1), eaao1749 (2018).
71. M. C. Sherrott, P. W. C. Hon, K. T. Fountaine, J. C. Garcia, S. M. Ponti, V. W. Brar, L. A. Sweatlock, and H. A. Atwater, "Experimental demonstration of >230 degrees phase modulation in gate-tunable graphene—Gold reconfigurable mid-infrared metasurfaces," Nano Lett. **17**(5), 3027–3034 (2017).
72. T. T. Kim, H. Kim, M. Kenney, H. S. Park, H. D. Kim, B. Min, and S. Zhang, "Amplitude modulation of anomalously refracted terahertz waves with gated-graphene metasurfaces," Adv. Opt. Mater. **6**(1), 1700507 (2018).
73. W. Liu, B. Hu, Z. Huang, H. Guan, H. Li, X. Wang, Y. Zhang, H. Yin, X. Xiong, J. Liu, and Y. Wang, "Graphene-enabled electrically controlled terahertz meta-lens," Photonics Res. **6**(7), 703–708 (2018).
74. Q. Li, X. Cai, T. Liu, M. Jia, Q. Wu, H. Zhou, H. Liu, Q. Wang, X. Ling, C. Chen, F. Ding, Q. He, Y. Zhang, S. Xiao, and L. Zhou, "Gate-tuned graphene meta-devices for dynamically controlling terahertz wavefronts," Nanophotonics **11**(9), 2085–2096 (2022).
75. N. Ullah, W. Liu, G. Wang, Z. Wang, A. U. R. Khalid, B. Hu, J. Liu, and Y. Zhang, "Gate-controlled terahertz focusing based on graphene-loaded metasurface," Opt. Express **28**(3), 2789–2798 (2020).
76. J. Huang, H. Guan, B. Hu, G. Wang, W. Liu, Z. Wang, J. Liu, Y. Zhang, and Y. Wang, "Enhanced terahertz focusing for a graphene-enabled active metalens," Opt. Express **28**(23), 35179–35191 (2020).
77. Z. K. Zhang, X. Q. Qi, J. F. Zhang, C. C. Guo, and Z. H. Zhu, "Graphene-enabled electrically tunability of metalens in the terahertz range," Opt. Express **28**(19), 28101–28112 (2020).
78. F. Lu, B. Liu, and S. Shen, "Infrared wavefront control based on graphene metasurfaces," Adv. Opt. Mater. **2**(8), 794–799 (2014).
79. E. Carrasco, M. Tamagnone, J. R. Mosig, T. Low, and J. Perruisseau-Carrier, "Gate-controlled mid-infrared light bending with aperiodic graphene nanoribbons array," Nanotechnology **26**(13), 134002 (2015).
80. Z. Li, K. Yao, F. Xia, S. Shen, J. Tian, and Y. Liu, "Graphene plasmonic metasurfaces to steer infrared light," Sci. Rep. **5**(1), 12423 (2015).
81. T. Yatooshi, A. Ishikawa, and K. Tsuruta, "Terahertz wavefront control by tunable metasurface made of graphene ribbons," Appl. Phys. Lett. **107**(5), 053105 (2015).
82. L. Luo, K. Wang, K. Guo, F. Shen, X. Zhang, Z. Yin, and Z. Guo, "Tunable manipulation of terahertz wavefront based on graphene metasurfaces," J. Opt. **19**(11), 115104 (2017).
83. W. Yao, L. Tang, J. Wang, C. Ji, X. Wei, and Y. Jiang, "Spectrally and spatially tunable terahertz metasurface lens based on graphene surface plasmons," IEEE Photonics J. **10**(4), 1–8 (2018).
84. S. R. Biswas, C. E. Gutiérrez, A. Nemilentsau, I. H. Lee, S. H. Oh, P. Avouris, and T. Low, "Tunable graphene metasurface reflectarray for cloaking, illusion, and focusing," Phys. Rev. Appl. **9**(3), 034021 (2018).
85. X. Shang, L. Xu, H. Yang, H. He, Q. He, Y. Huang, and L. Wang, "Graphene-enabled reconfigurable terahertz wavefront modulator based on complete Fermi level modulated phase," New J. Phys. **22**(6), 063054 (2020).
86. G. K. Shirmanesh, R. Sokhoyan, P. C. Wu, and H. A. Atwater, "Electro-optically tunable multifunctional metasurfaces," ACS Nano **14**(6), 6912–6920 (2020).
87. H. Cheng, S. Q. Chen, P. Yu, W. W. Liu, Z. C. Li, J. X. Li, B. Y. Xie, and J. G. Tian, "Dynamically tunable broadband infrared anomalous refraction based on graphene metasurfaces," Adv. Opt. Mater. **3**(12), 1744–1749 (2015).
88. P. Ding, Y. Li, L. Shao, X. Tian, J. Wang, and C. Fan, "Graphene aperture-based metalens for dynamic focusing of terahertz waves," Opt. Express **26**(21), 28038–28050 (2018).
89. J. He, R. Chen, Y. Li, S. Chen, Z. Liu, and Q. Zhang, "Graphene metalens with dynamic focusing and plane focusing in the terahertz range," Appl. Opt. **60**(20), 5752–5758 (2021).

Optical Materials EXPRESS

90. Z. Liu and B. Bai, "Ultra-thin and high-efficiency graphene metasurface for tunable terahertz wave manipulation," Opt. Express **25**(8), 8584–8592 (2017).
91. L. Liu, Y. Zarate, H. T. Hattori, D. N. Neshev, I. V. Shadrivov, and D. A. Powell, "Terahertz focusing of multiple wavelengths by graphene metasurfaces," Appl. Phys. Lett. **108**(3), 031106 (2016).
92. Z. Su, X. Chen, J. Yin, and X. Zhao, "Graphene-based terahertz metasurface with tunable spectrum splitting," Opt. Lett. **41**(16), 3799–3802 (2016).
93. B. Xiao, Y. Zhang, S. Tong, J. B. Yu, and L. Xiao, "Novel tunable graphene-encoded metasurfaces on an uneven substrate for beam-steering in far-field at the terahertz frequencies," Opt. Express **28**(5), 7125–7138 (2020).
94. S. AbdollahRamezani, K. Arik, S. Farajollahi, A. Khavasi, and Z. Kavehvash, "Beam manipulating by gate-tunable graphene-based metasurfaces," Opt. Lett. **40**(22), 5383–5386 (2015).
95. W. Ma, Z. Huang, X. Bai, P. Zhan, and Y. Liu, "Dual-band light focusing using stacked graphene metasurfaces," ACS Photonics **4**(7), 1770–1775 (2017).
96. S. E. Hosseininejad, K. Rouhi, M. Neshat, R. Faraji-Dana, A. Cabellos-Aparicio, S. Abadal, and E. Alarcón, "Reprogrammable graphene-based metasurface mirror with adaptive focal point for THz imaging," Sci. Rep. **9**(1), 2868 (2019).
97. M. Mittendorff, S. Winnerl, and T. E. Murphy, "2D THz Optoelectronics," Adv. Opt. Mater. **9**(3), 2001500 (2021).
98. X. Cai, A. B. Sushkov, M. M. Jadidi, L. O. Nyakiti, R. L. Myers-Ward, D. K. Gaskill, T. E. Murphy, M. S. Fuhrer, and H. D. Drew, "Plasmon-enhanced terahertz photodetection in graphene," Nano Lett. **15**(7), 4295–4302 (2015).
99. V. W. Brar, M. C. Sherrott, M. S. Jang, S. Kim, L. Kim, M. Choi, L. A. Sweatlock, and H. A. Atwater, "Electronic modulation of infrared radiation in graphene plasmonic resonators," Nat. Commun. **6**(1), 7032 (2015).
100. Y. Li, P. Ferreyra, A. K. Swan, and R. Paiella, "Current-driven terahertz light emission from graphene plasmonic oscillations," ACS Photonics **6**(10), 2562–2569 (2019).
101. Y. Li and R. Paiella, "Terahertz radiation processes in critically coupled graphene plasmonic nanostructures," J. Appl. Phys. **128**(15), 153105 (2020).
102. C. F. Bohren and D. R. Huffman, *Absorption and Scattering of Light by Small Particles* (Wiley-VCH, 2004).
103. M. Freitag, M. Steiner, Y. Martin, V. Perebeinos, Z. Chen, J. C. Tsang, and P. Avouris, "Energy dissipation in graphene field-effect transistors," Nano Lett. **9**(5), 1883–1888 (2009).
104. I. Kaminer, Y. T. Katan, H. Buljan, Y. Shen, O. Ilic, J. J. López, L. J. Wong, J. D. Joannopoulos, and M. Soljačić, "Efficient plasmonic emission by the quantum Čerenkov effect from hot carriers in graphene," Nat. Commun. **7**(1), ncomms11880 (2016).
105. V. Ryzhii, M. Ryzhii, and T. Otsuji, "Negative dynamic conductivity of graphene with optical pumping," J. Appl. Phys. **101**(8), 083114 (2007).
106. F. Rana, "Graphene terahertz plasmon oscillators," IEEE Trans. Nanotechnol. **7**(1), 91–99 (2008).
107. S. Boubanga-Tombet, S. Chan, T. Watanabe, A. Satou, V. Ryzhii, and T. Otsuji, "Ultrafast carrier dynamics and terahertz emission in optically pumped graphene at room temperature," Phys. Rev. B **85**(3), 035443 (2012).
108. D. Yadav, G. Tamamushi, T. Watanabe, J. Mitsushio, Y. Tobah, K. Sugawara, A. A. Dubinov, A. Satou, M. Ryzhii, V. Ryzhii, and T. Otsuji, "Terahertz light-emitting graphene-channel transistor toward single-mode lasing," Nanophotonics **7**(4), 741–752 (2018).

128.197.29.252 {ts '2022-11-09 10:27:26'}